

1 **An experiment to test satellite radar interferometry-observed geodetic ties**
2 **to remotely monitor vertical land motion at tide gauges**

3

4 M.S. Filmer¹, S.P.D. Williams², C.W. Hughes^{2,3}, G. Wöppelmann⁴,

5 W.E. Featherstone¹, P.L. Woodworth², A.L. Parker^{1,5}

6

7 1. School of Earth and Planetary Sciences, Curtin University, GPO Box U1987, Perth, WA 6845, Australia

8 2. National Oceanography Centre, Joseph Proudman Building, 6 Brownlow Street, Liverpool, L3 5DA, UK

9 3. School of Environmental Sciences, University of Liverpool, Liverpool, L69 3GP, UK

10 4. Littoral, Environment and Societies (LIENS), University of La Rochelle – National Centre for Scientific

11 Research (CNRS), 2 rue Olympe de Gouges, 17000 La Rochelle, France

12 5. Centre for Earth Observation, CSIRO Astronomy and Space Science, 26 Dick Perry Avenue, Kensington,

13 WA 6155, Australia

14 Corresponding author: M.Filmer@curtin.edu.au

15

16 ORCIDs

17 M.S. Filmer: <http://orcid.org/0000-0002-3555-4869>

18 S.P.D. Williams: <http://orcid.org/0000-0003-4123-4973>

19 C.W. Hughes: <http://orcid.org/0000-0002-9355-0233>

20 G. Wöppelmann: <http://orcid.org/0000-0001-7178-2503>

21 W.E. Featherstone: <http://orcid.org/0000-0001-9644-4535>

22 P.L. Woodworth: <http://orcid.org/0000-0002-6681-239X>

23 A.L. Parker: <http://orcid.org/0000-0003-4342-9301>

24

25

26

27

28 **Abstract:** The nature and linearity of vertical land motion (VLM) impacting the global sea
29 level record from tide gauges is not well known, but remains of importance to understand
30 long-term changes to sea level. Local surveys are required to directly measure VLM at tide
31 gauges relative to a global reference frame, but this is limited by the lack of differential VLM
32 measurements between tide gauges and continuously operating GPS (cGPS) stations that are
33 not co-located, i.e., fixed to the tide gauge structure. We present results from an experiment
34 using satellite radar interferometry (InSAR) scenes acquired from the TerraSAR-X satellite
35 mission to test whether InSAR could replace repeat geodetic levelling as a ‘geodetic tie’
36 between cGPS stations and tide gauges. Comparisons are made among TerraSAR-X (TSX),
37 cGPS and tide gauge minus altimetry VLM estimates for the Hillarys and Fremantle tide
38 gauges (Perth, Western Australia), which are used as test sites for this method. The results
39 suggest agreement between differential TSX and altimetry minus tide gauge VLM rates, but
40 systematic offsets among the absolute/geocentric rates where the TSX is referenced to IGS08
41 at the PERT cGPS. The TerraSAR-X VLM at the Fremantle tide gauge for the period 7
42 October 2012 – 7 October 2017 is $+0.45 \pm 0.40$ mm/yr (referenced to IGS08 at PERT cGPS),
43 although this should be treated cautiously over this short period, and also that VLM at
44 Fremantle and Hillarys appear to be non-linear over time. We infer from this that the
45 uncertainties in TerraSAR-X differential VLM rates are comparable to those from the highest
46 quality repeat levelling, although the uncertainty approaches ± 1 mm/yr if the reference point
47 uncertainty of the TSX and cGPS are considered when transformed to a terrestrial reference
48 frame.

49
50 **Key words:** InSAR, sea level change, vertical land motion, tide gauges

51
52
53
54
55
56

57 **1. Introduction**

58 Estimates of sea level change (SLC) rates and their de/acceleration determined by tide gauges
59 fixed to the Earth's surface are susceptible to vertical land motion (VLM), i.e., subsidence or
60 uplift, at their locations. Studies have focussed on these effects on global (e.g., Wöppelmann
61 and Marcos 2016; Hamlington et al. 2016; Santamaría-Gómez et al. 2017) and local (e.g.,
62 Raucoules et al. 2013; Wöppelmann et al. 2013; Featherstone et al. 2015; Bekaert et al. 2017;
63 Poitevin et al. 2019) scales. Tide gauges undergoing subsidence will imply an inflated rate of
64 sea level rise, and those experiencing uplift will show a lower rate of sea level rise, and
65 potentially sea level fall if the uplift is larger than the magnitude of long-term sea level rise,
66 such as in Fennoscandia and northern North America (e.g., Mazzotti et al. 2008). An
67 additional complexity is that non-linear VLM may imply artificial acceleration or
68 deceleration, or simply mask any real change in the linear rate of SLC.

69 Tide gauge VLM can be caused by anthropogenic effects due to
70 groundwater/fluid/gas extraction (e.g., Fielding et al. 1998; Brooks et al. 2007; Raucoules et
71 al. 2013) or natural variation at regional scale due to tectonics, glacial isostatic adjustment
72 (GIA), or a combination of some or all (e.g., Wöppelmann and Marcos 2016). Various
73 methods have been used to estimate tide gauge VLM, including the use of continuous GPS
74 (cGPS) stations at or near tide gauges (Bevis et al. 2002), GIA models (Peltier 2004), and
75 subtraction of satellite altimetry measurements of the sea surface adjacent to the tide gauge
76 from the sea level recorded by the tide gauge (Kuo et al. 2004). In the latter, the difference is
77 taken to be VLM at the tide gauge, on the assumption that the altimetry and tide gauge sea
78 level records should be observing the same sea level rate in the absence of any artefacts
79 (Wöppelmann and Marcos, 2016).

80 While all of these methods provide estimates of tide gauge VLM, they have
81 limitations, either in their measurement and processing, or that they may not be directly

82 measuring VLM at the tide gauge. For example, cGPS may be placed near tide gauges, but
83 still a kilometre or more away (e.g., King et al. 2012), so that local differential VLM between
84 the cGPS station and the tide gauge will mean that the VLM rate from the cGPS time series
85 may be different to the actual rate at the tide gauge (e.g., Featherstone et al. 2015). The
86 conventional method of monitoring differential VLM between the tide gauge and a cGPS
87 station is by repeat differential levelling, which as a quality control for first order standard
88 surveys usually has a maximum allowable misclosure of $2\sqrt{d}$ mm (d is the one way distance
89 between levelling endpoints in km) for two-way levelling forward and reverse between
90 benchmarks. Note, though, that levelling measures differential VLM relative to a geopotential
91 surface. When the geopotential is also changing, this can differ from the purely geometric
92 definitions of VLM from other techniques. In general, it is expected that these differences
93 will be negligible over a few kms compared to the differential VLM itself.

94 An example of the precision of high quality levelling is Lyon et al. (2018), who used
95 an east-west repeat levelling traverse across the Perth Basin to demonstrate that when best
96 practice in field and processing procedures are followed, a misclosure precision of $\sim 0.45\sqrt{d}$
97 mm can be achieved. This standard of levelling was shown to achieve rate uncertainties of
98 between ± 0.10 mm/yr and ± 1.87 mm/yr over four years for a 65-benchmark ~ 40 km long
99 repeat levelling line. The median for these uncertainties is ± 0.44 mm/yr, which could be
100 considered a best case precision over a ~ 4 year levelling time series, with two repeat surveys
101 conducted each year. Woodworth et al. (2017) refer to a repeat levelling connection between
102 a tide gauge and a cGPS station as a 'geodetic tie', however, this connection is often not done
103 by the agencies usually tasked with the surveys, usually due to funding/resource constraints
104 and the perceived low priority placed on these ties.

105 A feasible alternative to determine differential VLM between tide gauges and cGPS
106 stations is shown here through the use of satellite-borne InSAR (interferometric synthetic

107 aperture radar), and more specifically, methods such as persistent scatterer interferometry
108 (PSI) (e.g., Feretti et al. 2000; Kampes 2006; Hooper et al. 2007), and/or small baseline
109 multi-temporal InSAR (MTI; Hooper 2008; Hooper et al 2012). InSAR has been
110 demonstrated to estimate line of sight (LoS to satellite) land displacement at 1 mm/yr
111 precision, or in some circumstances less, depending on the number of SAR scenes and length
112 of the time series (e.g., Rucci et al. 2012; Cao et al. 2018). There have been a number of
113 InSAR studies that have investigated coastal VLM, including near tide gauges, e.g., Brooks et
114 al. (2007) in the Los Angeles area, Adamska (2012) at tide gauges in the UK, Raucoules et al.
115 (2013) in Manila, the Philippines, Wöppelmann et al. (2013) in Alexandria, Egypt, Le
116 Cozannet et al. (2014; 2015) in Dakar, Senegal, Bekaert et al. (2017) in the Chesapeake Bay
117 region of the USA, and Poitevin et al. (2019) at Brest, France. All of these have used InSAR
118 to estimate VLM in the coastal area surrounding the tide gauge(s), inferring VLM at the tide
119 gauge. However, they have not used them as a dedicated geodetic tie between a cGPS and the
120 tide gauge, as we propose and test here.

121 We describe experiments using five integer years of SAR acquisitions from the
122 German Aerospace Center's (DLR's) TerraSAR-X (TSX) satellite mission over a test site
123 containing the Fremantle (FREM) and Hillarys (HILS) tide gauges in Perth (Australia). These
124 tide gauges are suitable for this experiment because (1) HILS has a co-located cGPS (fixed to
125 the tide gauges structure) that can be used for validation, (2) FREM has a long running (>100
126 year) tide gauge record, and (3) the tide gauges are only ~30 km apart, so can be used to test
127 the differential VLM between them on the assumption that the SLC signal at both tide gauges
128 are the same. HILS is known to be undergoing non-linear VLM (Featherstone et al. 2015),
129 while Featherstone et al. (2015) has suggested FREM is also undergoing non-linear VLM (cf.
130 Thompson and Merrifield 2018; Burgette et al. 2013).

131 Other SAR scenes are available over the test site, e.g., C-band scenes from the
132 European Space Agency's Envisat and Sentinel-1 satellite missions, but neither provide a
133 sufficiently long time series nor the number of scenes that we have available from TSX. For
134 example, Sentinel-1A started acquisitions in 2014 and observed the test site for an eight
135 month period (e.g., Parker et al. 2017), while Sentinel-1B did not begin observations until
136 2016. Comparisons between X-band and C-band displacements in Parker et al. (2017)
137 indicated reasonable agreement between these data although over a very short period, so are
138 not conclusive. Using 141 TSX scenes acquired between 7 October 2012 and 7 October 2017
139 (herein referred to by decimal years 2012.8-2017.8 to denote five integer years), we have
140 estimated VLM rates at these tide gauges in the test site to determine the utility of InSAR to
141 monitor differential VLM between tide gauges and cGPS stations as an alternative to
142 differential levelling for the geodetic tie.

143 Repeat differential levelling and InSAR are two different relative measurement
144 techniques: levelling measures multiple short-distance (maximum of ~40 m sight length)
145 height differences from ground-based instruments set up orthogonal to the local gravity
146 vector (e.g., Vaníček et al. 1980), while InSAR measures the geometric off-nadir LoS using
147 radar backscatter from the Earth's surface back to the satellite (see e.g., Hanssen 2001) from
148 repeat orbits (e.g., 11 days for TSX). Hence, repeat levelling measures the height difference
149 between specific points on land during separate surveys (ideally four times per year for VLM
150 monitoring) with respect to the local gravity vector, but InSAR measures the changes in LoS
151 range between the ground (over a 'pixel', not a specific point) and the satellite for multiple
152 pixels within the scene (50 km x 30 km for TSX stripmap). The processed InSAR LoS
153 ranges, and repeat levelling surveys produce displacement time series, but at different spatial
154 and temporal resolution with their own specific measurement and error characteristics. Both

155 time series can be used to estimate rates of VLM at tide gauges, relative to a cGPS station, as
156 we demonstrate for InSAR.

157 Mahapatra et al. (2018) used a radio transponder co-located at a tide gauge in the
158 Netherlands to determine InSAR VLM rates relative to the tide gauge and co-located cGPS.
159 However, tide gauge co-located InSAR ground infrastructure, such as transponders and
160 corner reflectors (CRs) are not available at most global tide gauges, all of which need
161 monitoring for VLM to estimate accurate rates of SLC. Indeed, Wöppelmann and Marcos
162 (2016) report that only 14% of the Global Sea Level Observing System (GLOSS) tide gauges
163 have co-located cGPS stations (i.e., fixed directly to the tide gauge structure), so that
164 differential VLM for the tide gauges where cGPS is not co-located will need to be monitored.
165 While the use of transponders and CRs may provide improved location accuracy (e.g.,
166 Mahapatra et al., 2014; Dheenathayalan et al. 2016; 2017; Garthwaite 2017), these are not
167 likely to be available on a global scale for some years, and perhaps never for countries that
168 cannot afford such infrastructure. Hence, we test differential InSAR to tide gauges as an
169 alternative technique that could potentially be applied globally, depending on the availability
170 of SAR imagery.

171

172 **2. Methods and data**

173 The data used and processing methods described in this section are arranged with a sub-
174 section for each technique. The cGPS in the test site (International GNSS Service (IGS) code
175 PERT; Figure 1), is used to transform the InSAR displacement time series to a terrestrial
176 reference frame (TRF) – IGS08 for this experiment – which is aligned with the International
177 reference Frame 2008 (ITRF2008; Altamimi et al. 2011). Derived TSX IGS08 rates can then
178 be compared to cGPS IGS08 rates at other locations for validation, and the TSX rates at each
179 tide gauge are then in a known TRF.

180 We use PERT as the single reference point because it is considered the most reliable
181 site for (1) cGPS time series (since 1995) and (2) the TSX reference pixel nearest to the
182 cGPS. This is compared to HIL1 which is co-located with HILS but located on the roof of the
183 tide gauges shed on a jetty in a boat harbour full of moored yachts with tall masts (possibly
184 causing multipath) and has a break in its time series (Figure 2B). CUIAI is mounted atop a 4-
185 story building, which may not be stable, nor a reliable site for TSX backscatter from the
186 cGPS location.

187

188 **2.1 InSAR**

189 We first processed the 141 TSX scenes using the small baseline multi-temporal InSAR (MTI)
190 method implemented in the Stanford Method of Persistent Scatterer (StaMPS; Hooper et al.
191 2012) software as described in Hooper (2008). The interferograms were processed using
192 Doris (Delft object-oriented radar interferometric software; Kampes and Usai 1999), forming
193 705 small baseline interferograms. The small baselines interferogram pairs were selected
194 manually, with the objective of keeping perpendicular (i.e., the distance between repeat
195 satellite positions, orthogonal to the LoS) and temporal baselines as small as possible, but
196 retaining redundancy in the network so that each scene was connected by at least three small
197 baseline interferograms.

198 The high redundancy small baselines help reduce the effect of temporally variable
199 tropospheric noise (Williams 1998; Agram and Simons 2015; Fattahi and Amelung 2015;
200 Cao et al. 2018). Residual time correlated noise in the TSX time series was identified and
201 accounted for in the time series analysis in section 3.2. The TSX phase ramp was estimated
202 and used to remove the long-wavelength orbit and ionosphere effects that may be present in
203 the TSX scene extent of 50 km x 30 km. This is appropriate for extents of <100 km (Hooper
204 et al. 2012), but also because X-band is less affected by the ionosphere (cf. Gomba et al.

205 2017), TSX orbit errors are relatively small (Fattahi and Amelung 2014), and the study area
 206 is relatively flat, so less affected by stratified tropospheric effects (Bekaert et al. 2015).

207 The TSX slowly-decorrelating filtered phase (SDFP; Hooper 2008) pixels (stripmap
 208 spatial resolution ~ 3 m) were down-sampled to 30 m spatial resolution, using the method of
 209 Hooper et al. (2012), resulting in 827,215 points. The pixels were down-sampled to reduce
 210 the computing load and smooth noisy pixels, and were calculated using nearby pixels
 211 weighted from their signal-to-noise ratio (Hooper et al. 2012). We conducted earlier
 212 experiments with the individual TSX SDFP pixels for the 4-year 2012.7-2016.7 time series
 213 (10,175,104 versus 728,702 down-sampled pixels), which indicated that the rates from the
 214 down-sampled pixels were more reliable when tested with independent results (i.e., cGPS and
 215 altimetry minus tide gauge VLM rates). For this reason, the down-sampled pixels were used
 216 in this experiment, and referred to herein as DPs. The TSX phase differences were
 217 unwrapped using 3D phase unwrapping (Hooper et al. 2007), and initially relate to an
 218 arbitrary datum where the mean of all velocities is taken as the zero reference.

219 The small baseline $m \times n$ array comprises unwrapped DP phase differences ($\Delta\phi$),
 220 where m is the number of DPs (827,215) and n is the number of small baseline
 221 interferograms (705). To compute relative displacements for each DP per scene acquisition
 222 (t_a), which is 140 for this time series (first column of 141 scenes is removed; see below), a
 223 coefficient matrix \mathbf{G} ($n \times p$) is formed that describes the functional relation between the small
 224 baseline interferograms and the number (p) of t_a (705 \times 140). The vector of phase
 225 displacements \mathbf{d} for each DP is computed row by row, where $\Delta\phi = \mathbf{G}\mathbf{d}$ using Gaussian
 226 elimination to invert the matrix. Each successive computation of \mathbf{d} builds the $m \times p$
 227 displacement matrix \mathbf{D} . To remove the rank defect from \mathbf{G} , the first column is removed
 228 (leaving 140 from 141 scenes) so that the first acquisition becomes t_0 and is the zero
 229 reference for the time series of displacements. This means that the TSX time series

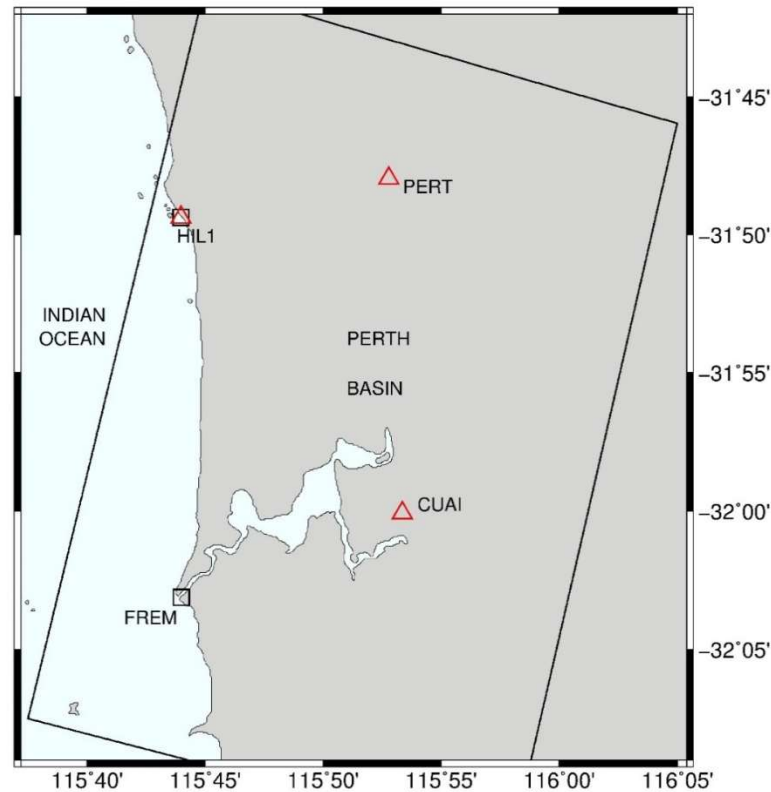
230 displacements will be relative to zero, so that although the displacement trends are
231 transformed relative to the IGS08 reference frame, TSX DPs do not become IGS08 heights.
232 The $D_{m,p}$ (827,215 x 140) displacement array is transformed to the TRF as per section 2.5.

233

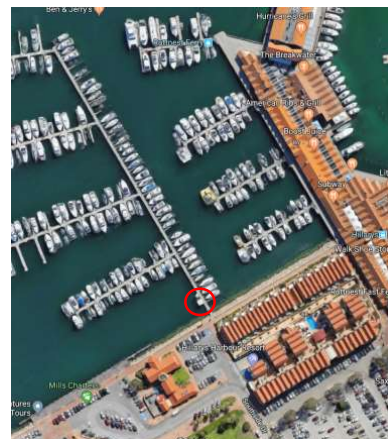
234 **2.2 GPS**

235 Daily cGPS positions were obtained from the Nevada Geodetic Laboratory (NGL;
236 <http://geodesy.unr.edu/NGLStationPages/GlobalStationList>; Blewitt et al. 2018). These data
237 were used to estimate time series velocities and realistic uncertainties using the CATS
238 software (Williams 2008). The spectral index was solved for the five-year TSX period
239 (2012.8-2017.8) using 11 cGPS receivers located on a building at Curtin University in
240 addition to PERT (pillar mounted) and HIL1 (co-located with HILS). The average spectral
241 index was -0.72 for all 13 cGPS time series, so this fixed spectral index was used to
242 recompute the trend with the annual and semi-annual terms and variable white noise. The
243 mean spectral index from all 13 cGPS time series was used to avoid introducing a bias in the
244 spectral indices at PERT and HIL1 that could have resulted from the shorter variable time
245 series. Only one of these building-mounted cGPS (CUAI; Figure 1) was used to provide an
246 additional cGPS comparison for the TSX, because it had the best quality time series (Figure
247 2C), while the others were all fixed to the same building, and some had incomplete and/or
248 gaps in their time series for the full TSX time period.

249



250
251



252

253 Figure 1: (Top) Map showing the test site, with cGPS stations (red triangles) and tide gauges

254 (black squares), with the extent of the TSX scene shown by the black line. cGPS CUAI is

255 located on top of a multi-storey building. (Bottom) FREM tide gauge (left), and HIL1 co-

256 located cGPS and HILS tide gauge (right) are shown in the red circles. Bottom images

257 sourced from Google Imagery (2019).

258 *2.3 Tide gauge sea level*

259 Monthly mean sea level values from the Permanent Service for Mean Sea Level

260 (PSMSL, Holgate et al 2013) were used for 1993.0–2018.0 (altimeter period) and for 2012.8–

261 2017.8 (TSX period) to compare InSAR VLM rates to (1) tide gauge minus altimetry VLM at
262 HILS and FREM, and (2) to differential tide gauge minus altimetry VLM rates between these
263 gauges. HILS and FREM are ~30 km apart (Figure 1), where any difference in SLC is
264 assumed to be due to relative tide gauge VLM (e.g., Burgette et al. 2013), so this will be used
265 to provide some additional evidence to support the TSX differential VLM (but not absolute
266 VLM in the IGS08 TRF). In creating the gridded altimeter product, a dynamic atmosphere
267 correction has been applied by AVISO. This accounts for the inverse barometer effect at all
268 periods, and for barotropic ocean dynamics at periods shorter than 20 days. For consistency
269 among the tide gauge and altimetry data, the same correction was also applied to each of the
270 tide gauge time series, as extracted from the nearest grid point of the ocean model output. The
271 effect of long period tides (Woodworth, 2012) was found to be below 0.03 mm/yr and was
272 thus neglected.

273 The CATS software was first used to estimate rates and uncertainties for the full sea
274 level records at both tide gauges as a check on the results and data. The power law index was
275 -0.96 for the full (>100 year) FREM record, indicating flicker noise. Similar results were
276 obtained for HILS, with a power law index of -1.14 for the full (~ 25 year) record. To avoid a
277 possible bias in the sea level rates from using a spectral index computed from a short period
278 time series, the five-year rates were recomputed in CATS with the power law index fixed at
279 -0.96 , on the assumption that the true spectral index of two tide gauges close together should
280 be very similar.

281 ***2.4 Altimetry sea level***

282 To compare the InSAR-derived VLM, tide gauge sea level observations minus
283 satellite altimetry observations near the tide gauge can be used to estimate VLM at the tide
284 gauge (e.g., Pfeffer and Allemand 2016; Wöppelmann and Marcos 2016, and many others).
285 Altimetry data from AVISO (the Ssalto/Duacs, delayed mode, gridded absolute dynamic

286 topography product using all available satellites, and with a dynamic atmosphere correction
287 applied as described above) was used to estimate monthly sea surface heights adjacent to the
288 two tide gauges. Data were extracted from the grid point within 200 km of the tide gauge
289 which explains most of the variability seen at the tide gauge. This is a compromise, designed
290 to limit the effect of increased instrumental and sampling errors near the coast, balanced
291 against the inevitable loss of some near-coastal signal, and inevitable (and time dependent, as
292 the satellite systems evolve over time) limitation of the satellite measurement system. Tide
293 gauge sea level monthly means were subtracted from altimetry monthly means with the VLM
294 rates estimated using CATS from the differenced time series for the full altimeter record
295 (1993.0-2018.0) and for the TSX period (2012.8-2017.8), after accounting for annual and
296 semi-annual terms. This method assumes that, apart from any seasonal cycle, altimetry sea
297 level realises the ‘true’ SLC rate at the tide gauge, with the difference to tide gauge sea level
298 interpreted as the VLM at the tide gauge, with other errors (e.g., altimetry observation and
299 processing errors) assumed negligible. Wöppelmann and Marcos (2016) estimated global tide
300 gauge minus satellite altimetry uncertainties of up to ± 3 mm/yr, but with a median of ± 1
301 mm/yr from a set of 478 selected global tide gauges.

302

303 ***2.5 Transformation of InSAR time series to TRF***

304 Transforming the TSX LoS rates into a TRF is important so that the rates from different
305 measurement techniques (i.e., GPS, InSAR and altimetry) can be directly compared (cf.
306 Wöppelmann et al. 2007; Bekaert et al. 2017; Hammond et al. 2018; Mahapatra et al. 2018).
307 Using the S-transform method from Mahapatra et al. (2018) for a large data set, the \mathbf{I} matrix
308 ($m \times m$) becomes large, and we found the $m = 827,215$ array to be beyond available computer
309 memory. An alternative method was therefore implemented, where the TSX reference point
310 (RP) displacement row vector \mathbf{d}_{RP} is subtracted from all \mathbf{d}_i , (DP displacement vectors held in

311 the displacement matrix \mathbf{D}) where \mathbf{d}_{RP} is given a (temporary) arbitrary zero displacement for
 312 all acquisition times (t_a). This produces the same results as the S-transform method but is
 313 done as a direct operation on \mathbf{D} and does not require the computation of the large \mathbf{I} .

314 The \mathbf{d}_i are then transformed to the TRF through the connection between \mathbf{d}_{RP} and the
 315 cGPS time series, which are treated as co-located (cf. Figure 2A). The velocity is computed
 316 from the cGPS time series (Section 2.2) for the same period as the InSAR \mathbf{d}_{DP} (2012.8-
 317 2017.8) so that the \mathbf{d}_i time series transformed as (Mahapatra et al. 2018)

$$318 \quad \mathbf{d}_{i,TRF} = \mathbf{d}_i + \mathbf{H}\mathbf{d}_{GPS} \quad (1)$$

319 where $\mathbf{d}_{i,TRF}$ is \mathbf{d}_i related to the TRF. \mathbf{H} is a vector constraint to set the datum of a free
 320 network (here comprising ones whereby the average of all displacements is taken as the
 321 reference) and \mathbf{d}_{GPS} is the vector of linear displacements at each TSX t_a from the estimated
 322 cGPS trend connecting the InSAR DPs to the TRF computed as

$$323 \quad \mathbf{d}_{GPS} = v_{GPS} \times (t_a - t_0)/365.25 \quad (2)$$

324 where v_{GPS} is the estimated linear velocity of the cGPS time series in mm/yr and $(t_a - t_0)$ is
 325 the period (days) over which v_{GPS} is computed, then converted to years by dividing by
 326 365.25. The resulting displacement array \mathbf{D}_{TRF} comprises row vectors $\mathbf{d}_{i,TR}$ representing
 327 each DP displacement transformed into the TRF. The TSX rate and uncertainty can then be
 328 computed from $\mathbf{d}_{i,TRF}$ at the tide gauge locations.

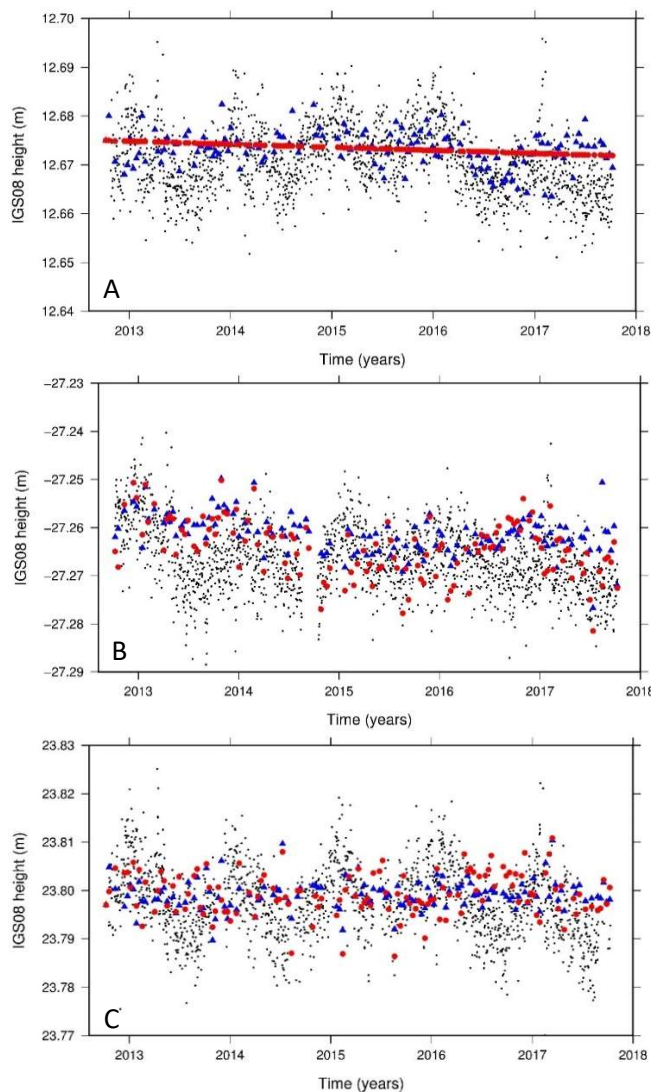
329

330 **3. Results and Discussion**

331 **3.1 Time series comparisons**

332 Initial comparisons were made between the cGPS and TSX time series as a check. Figure 2
 333 shows the cGPS time series at PERT, HIL1 and CUA1 compared to their nearest TSX DP
 334 before and after transformation to IGS08 constrained to the CATS-estimated cGPS IGS08
 335 rate at the RP (PERT). The linear rate (red dots in Figure 2A) represents the transformed TSX

336 rate, which is now coincident with the cGPS rate. The pre-transformation TSX time series
 337 (blue triangles) indicates that it is sensing similar VLM signals to the cGPS. The main
 338 differences are between the maximum amplitude of the cGPS annual periodic signal, where
 339 the TSX amplitudes are, generally lesser magnitude. This may be due to the different
 340 measurement and processing characteristics of the SAR and GPS systems. For instance, the
 341 TSX may be sensing a close-by, but different, feature to the cGPS structure, and also the
 342 filtering in the TSX processing may tend to over-smooth the seasonal amplitude when
 343 compared with the higher solution rate of the cGPS.



344

345

346

347 Figure 2: (A) PERT cGPS (IGS08) time series (black dots) compared to the time series for

348 the nearest TSX LoS DP before transformation (blue triangles) and after transformation (red

349 circles). (B) As for (A), but for HIL1 cGPS time series and nearest TSX LoS DP before and
350 after the rates have been transformed; (C) As for (B), but for CUIAI cGPS time series and
351 nearest TSX LoS DP. Note that the cGPS time series daily solutions are IGS08 heights, but
352 the TSX time series displacements are relative to zero, shifted on the y-axis to IGS08 heights
353 for plotting purposes to compare to the cGPS time series.

354

355 Both the TSX and GPS time series in Figure 2A suggest an uplift trend until 2016,
356 and then possibly subsiding after this, although this should be viewed cautiously for a
357 relatively short time series, and in the presence of the GPS seasonal signal. The HILS TSX
358 and HIL1 GPS time series in Figure 2B do not agree as well as at PERT, although there are
359 still similarities between them. HIL1 is a ‘noisier’ site than PERT (which is why PERT was
360 used as the reference point for the TRF), for both GPS and the TSX. because of the masts on
361 yachts moored nearby, and also because the TSX may not be sensing the tide gauge location
362 exactly (cf. Figure 1). Similar problems may be experienced at some global tide gauges
363 where this method may be applied.

364 The rate for the cGPS station (CUIAI) located on top of a multi-storey building at
365 Curtin University (Figure 1C) was also estimated as an additional comparison on the TSX.
366 Because a site on a building is not ideal due to possible building movement (e.g., thermal
367 expansion and contraction), and that the TSX DP may not sense the same position on the
368 building as the cGPS, it was used only as a check on the TSX VLM rates.

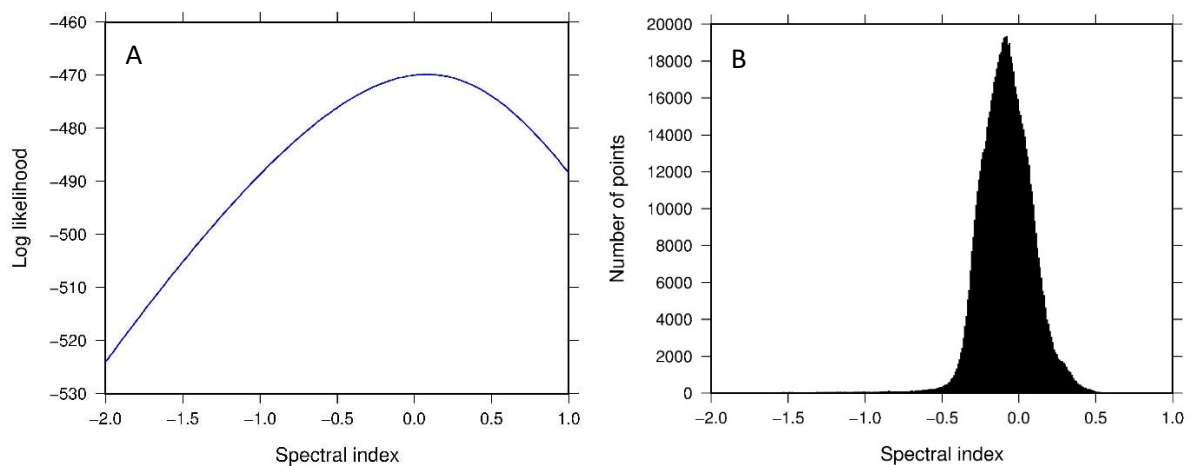
369

370 ***3.2 InSAR noise analysis***

371 The noise content in the residual TSX time series (following processing) is not known and
372 likely to be time-correlated. If unaccounted for it may introduce errors in the VLM rate and
373 certainly underestimate the rate uncertainty (Williams et al. 1998; Williams 2003; 2008). We

374 conducted an analysis of the time correlated noise in the TSX time series so that a more
 375 appropriate noise model could be applied to the estimation of the rate and rate uncertainty).
 376 The relatively short time series of five years and 141 epochs limits the number of resolvable
 377 parameters in the maximum likelihood estimation (MLE) so we used a power-law only model
 378 instead of a power-law plus white noise model more typically used in geophysical time series
 379 analysis. It is more important to capture the coloured noise aspects of the series than the
 380 white noise since this is what influences the rate uncertainty the greatest. We took a network-
 381 based approach where all 827,215 DPs in the SAR scene were included in to estimate the
 382 spectral index on the assumption that the TSX time series noise characteristics are the same
 383 across the scene and therefore provide a more robust estimate of the spectral index. To reduce
 384 the computational burden, a single covariance matrix was precomputed and applied to all
 385 827,215 DP time series in the image. A log-likelihood (LL) calculation was run on a range of
 386 spectral indices from -2 (random walk) to $+1$ (at 0.1 intervals) for all DP time series to find
 387 the maximum LL (Figure 3A) and then interpolated to get the best estimate of the spectral
 388 index for each DP time series.

389



390

391 Figure 3: (A) is the log-likelihood (LL) for TSX DP #1 as a function of spectral index. The

392 estimated spectral index is calculated from the largest LL and the two values either side. (B)

393 Histogram of spectral indices for each transformed TSX DP time series.

A: Simulated Spectral Index	B: Estimated Spectral Index
0.00	0.19 ± 0.19
-0.09	0.10 ± 0.18
-0.26	-0.08 ± 0.18
-0.50	-0.33 ± 0.18
-1.00	-0.85 ± 0.17

394

395 Table 1: Simulated fixed spectral index (column A) and spectral index estimated as the
 396 standard deviation of all DP time series in the TSX data (column B).

397

398 The spectral indices of all 827,215 DP time series is shown in Figure 3B, with a mean

399 value of -0.09 . The estimated spectral index from this five-year time series may be biased on

400 the low side (lesser magnitude, but negative value) because we remove a component of the

401 correlated signal together with the “true” slope when the slope is estimated. To test for a

402 possible bias, we simulated noise with a fixed spectral index and the same number of points

403 in the TSX data, then estimated the spectral index (Table 1, column A). The test indicates the

404 true spectral index from the data is likely to be larger in magnitude (but negative) than that

405 estimated and shown in Table 1. The range (highest to lowest) of the simulated estimates is

406 similar to those computed from the data (~ 1.0), so from Table 1 we adopt the estimated

407 spectral index value of -0.08 (closest to the computed value of -0.09) which is then related to

408 the corresponding simulated spectral index of -0.26 . A fixed spectral index of -0.26 is then

409 used in CATS for all TSX rate estimation.

410

411 **3.3 Sea level rates**

412 Linear rates of SLC from the tide gauges and altimetry for 1993.0-2018.0 and for the TSX

413 period 2012.8-2017.8 are shown in Table 2. The 1993.0-2018.0 SLC rates are included as a

414 comparison, with the shorter period being more affected by variability in short term sea level

415 (Woodworth et al. 2019). The short-term relative sea level rates are of less interest in this

416 study, but the differential rates between the tide gauge sites are used to support the validity of

417 the TSX VLM (Section 3.4). The tide gauge rates contain VLM that is dependent on the tide
 418 gauge site, and also the sea level signal. The altimetry measures only sea level at a location
 419 offshore from the tide gauge. Over a distance of only ~30 km, the sea level rate should be the
 420 same, as seen by the altimetry over the longer 1993.0 – 2018.0 period, so that the differential
 421 rate between the tide gauges is assumed to be primarily VLM. The tide gauge differential rate
 422 sums to ~47 mm over ~25 years, which compares to ~70 mm over 40 years in Featherstone et
 423 al. (2015) from repeat levelling. Both show HIL1 subsiding at a faster rate than FREM.

424

	SLC 1993.0-2018.0 (mm/yr)	SLC 2012.8-2017.8 (mm/yr)
FREM		
Tide gauge	+6.95±2.66	-11.90±9.67
Altimetry	+5.23±2.47	-14.52±9.77
HILS		
Tide gauge	+8.84±2.58	-13.96±10.04
Altimetry	+5.29±2.51	-18.49±9.48

425

426 Table 2: Tide gauge and altimetry sea level rates for FREM and HILS. The tide gauge rates
 427 contain the VLM and the ocean sea level signal, whereas the altimetry contains only the sea
 428 level ocean signal.

429

430 All VLM rates were computed using CATS, as described in Sections 2.2, 2.3 and 3.2.

431 The tide gauge minus altimetry VLM rates were estimated from the differenced monthly
 432 means (as per Section 2.4) so are slightly different to the differences of the rates shown here.

433 The differential tide gauge minus altimetry VLM rate between the tide gauges was also
 434 estimated from the double differences of the tide gauge and altimetry monthly means, which
 435 resulted in reduced uncertainties to those shown in Table 2. Double differencing was used
 436 only for the tide gauge and altimetry sea level measurements because the ocean contains large
 437 annual, interannual and decadal variabilities to which linear rates can be more sensitive than
 438 GPS and TSX rates.

439 **3.4 VLM rates**

440 The small baseline LoS phase differences were converted to VLM displacements for each DP
441 on the assumption that there is no relative horizontal motion among the cGPS and tide gauges
442 (indicated to be the case for this test site in Parker et al. 2017). All DP time series
443 displacements were then referenced to the TRF at the cGPS (PERT) using the methods
444 described in Section 2.5. Equations (1) and (2) were used to transform to the TRF through the
445 connection to the cGPS, using $v_{GPS} = -0.62 \pm 0.52$ mm/yr for PERT in the TRF. This cGPS
446 rate was estimated using CATS for 2012.7-2017.7 as per Section 2.2.

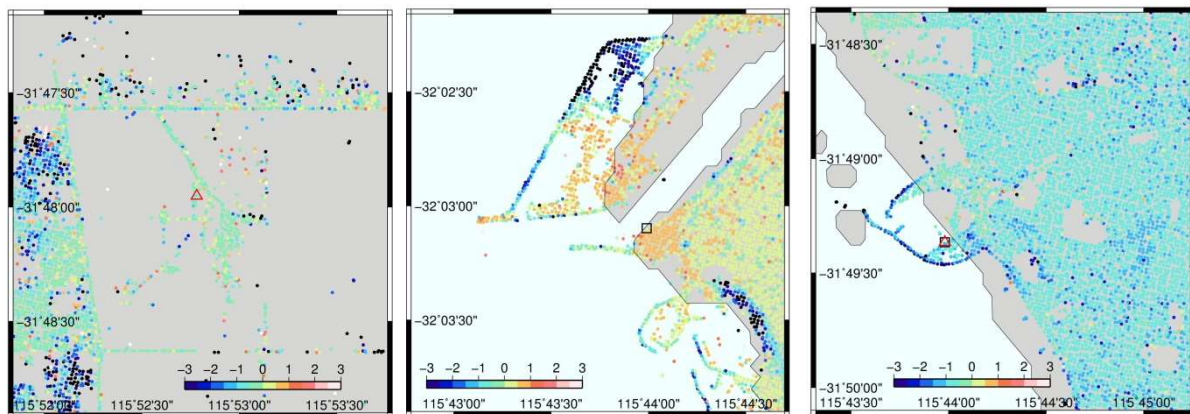
447 The TSX rates were computed in CATS using the fixed spectral index of -0.26
448 estimated in Section 3.2, variable white noise and annual and semi-annual terms. These rates
449 are shown in Figure 4, with Figure 4A showing DPs close to the cGPS (RP used is calculated
450 within 4 m) with rates between -0.5 mm/yr and -1.0 mm/yr (RP fixed to -0.62 mm/yr). This
451 indicates that the land surrounding the cGPS is subsiding at a similar rate to the cGPS
452 structure so that it is reasonable to adopt the closest DP as TSX RP in this case and supports
453 PERT's use as the RP for the TRF transformation.

454 Figure 4B shows the region adjacent to FREM to be uplifting in the range $+0.5$ mm/yr
455 to $+1.0$ mm/yr, but the location of the tide gauge itself is in the 0.0 mm/yr to $+0.5$ mm/yr
456 range (FREM $+0.45$ mm/yr). The area showing the higher uplift is covered by several
457 buildings, so these may be the dominant scatterers near this location. The subsidence
458 experienced by the coastal breakwater structure to the north of FREM is notable, as is the
459 area along the waterfront to the south. These comprise human-made structures that are liable
460 to settlement and subsidence. The areas without DPs are likely due to temporal decorrelation,
461 from vegetation changes or in the car parks and vehicle unloading/storage area on the docks
462 where the position and cars will not be the same for each SAR acquisition. The VLM in the
463 vicinity of Fremantle is variable, ranging from $+2$ mm/yr to <-3 mm/yr which reinforces the

464 need to monitor VLM at the tide gauge site, rather than simply adopt the rates from a remote
 465 cGPS station that is not co-located with the tide gauge.

466 The DPs near HIL1 and HILS (Figure 4C) also indicates consistency in the -1 mm/yr
 467 to -1.5 mm/yr range (HIL1 TSX rate at -1.20 mm/yr), which supports the adoption of the
 468 nearest DP. It is not clear if the DP adopted is actually sensing the tide gauge itself or the
 469 close by land (within ~ 5 m), but they do appear to be subsiding at similar rates.

470



471

472 Figure 4: TSX DP rates (mm/yr) around (A) PERT (red triangle); (B) FREM (black square);
 473 (C) HIL1 (red triangle), and co-located HILS tide gauge (black square).

474

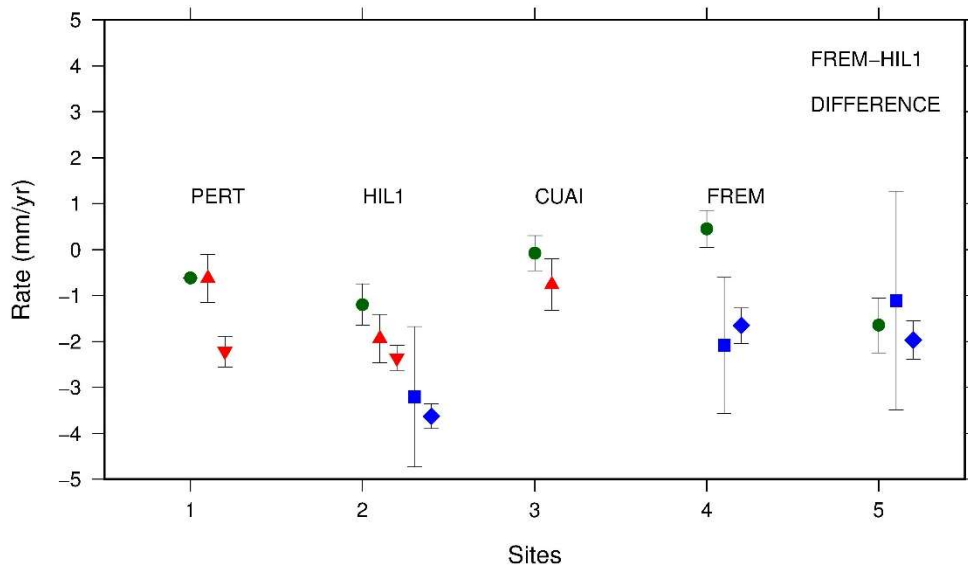
475 The VLM rates from the different measurement techniques are summarised in Figure
 476 5, and listed in Table 3. The difference between the 2012.8-2017.8 cGPS rates (red triangles)
 477 and the TSX rates (green circles) at HIL1 (cGPS -1.94 ± 0.53 mm/yr; TSX -1.20 ± 0.40
 478 mm/yr) and CUA1 (cGPS -0.78 ± 0.60 mm/yr; TSX -0.08 ± 0.38 mm/yr) indicate the precision
 479 of the TSX within the TRF. Although the agreement is at the edge of the respective error bars
 480 computed for the TSX time series (Figure 5), the differences are < 0.74 mm/yr, so less than
 481 the median uncertainty of ± 1 mm/yr for altimetry minus tide gauge VLM from the global
 482 study of Wöppelmann and Marcos (2016). The CATS-derived cGPS rates are both less than
 483 the CATS-derived TSX rates (larger subsidence for GPS), which indicates a bias, although

484 this cannot be certain for only two cGPS stations, one of which is building-mounted. The
485 TSX at FREM suggests small uplift of $+0.45 \pm 0.40$ mm/yr, which is barely significantly
486 different from zero VLM (cf. Burgette et al. 2013), but this is inclusive to the 2012.8-2017.8
487 period only, and care should be taken in making direct comparisons with VLM rates from
488 different periods, especially as some parts of the Perth Basin have experienced non-linear
489 subsidence (Featherstone et al. 2015).

490 It should also be considered that the uncertainties shown in Table 3 contain only the
491 TSX time series uncertainty at the site, so does not fully account for uncertainties in the cGPS
492 and TSX at the PERT RP, and the cGPS in the comparisons at HIL1 and CUIAI. A linear
493 error propagation may provide an upper bound approximation of the uncertainty if all the
494 related measurements are taken into account. Using the time series uncertainties in Table 3
495 for the PERT TSX (nominally zero) and cGPS, we propagate these to the FREM TSX rate,
496 getting ± 0.69 mm/yr, while for HIL1 we obtain ± 0.87 mm/yr, and CUIAI ± 0.88 mm/yr. The
497 CUIAI and HIL1 sites include their cGPS uncertainty in the linear error propagation. These
498 may be an upper bound, but suggest that the differences between cGPS and TSX at HIL1 and
499 CUIAI are within the uncertainty when the TRF RP is taken into account.

500 Longer period cGPS rates are shown in Table 4 that were computed using CATS and
501 NGL data for this study (shown in Figure 5), and also from the University of La Rochelle
502 processing (ULR6A, Santamaría-Gómez et al. 2017) and the Median Interannual Difference
503 Adjusted for Skewness (MIDAS) method (Blewitt et al. 2016). These are shown to provide
504 an additional comparison for the longer term cGPS and altimetry minus tide gauge VLM
505 rates thus serving as (1) a check for the other rates of similar periods, and (2) give an
506 indication whether there is non-linearity at the VLM at these sites when compared to different
507 time periods.

508



509
510

511 Figure 5: Velocity estimates (mm/yr) for TSX 2012.8-2017.8 (green circles), GPS 2012.8-
512 2017.8 (red triangles); longer term (see Table 4) cGPS rates computed for this study using
513 NGL data (inverted red triangles), and tide gauge minus altimetry VLM 2012.7-2017.7 (blue
514 squares) and 1993.0-2018.0 (blue diamonds). So-called ‘Site’ 5 actually shows the
515 differential VLM between HILS and FREM for TSX and tide gauge minus altimetry. See
516 Table 3 for numerical VLM rates.

517
518

519 The tide gauge minus altimetry VLM rates for 2012.8-2017.8 are -2.09 ± 1.48 mm/yr
520 and -3.21 ± 1.53 mm/yr (Table 3) for FREM and HILS, respectively, and appear to be
521 systematically larger subsidence rates than the TSX (~ 2 - 2.5 mm/yr more subsidence;
522 referenced to IGS08 at the PERT cGPS). These differences are statistically significant, and
523 also larger than the ± 1 mm/yr uncertainty estimate for tide gauge minus altimetry VLM from
524 Wöppelmann and Marcos (2016), suggesting that the constant offset may be a systematic bias
525 between the IGS08-referenced TSX and the tide gauge minus altimetry VLM. The cGPS
526 rates at HIL1 and CUA1 are closer to the TSX (~ 0.74 mm/yr) than the altimetry minus tide
527 gauge VLM at HILS (~ 1.2 mm/yr), suggesting that the TSX is slightly closer to the true
VLM rate, albeit on the assumption that cGPS is the most reliable technique for determining

528 VLM. In this comparison, the differential TSX is referenced to cGPS at PERT, so can be
 529 directly compared to cGPS processed in the IGS08 reference frame.

Site	TSX 2012.8-2017.8	cGPS 2012.8-2017.8	Alt-tide gauge 2012.8-2017.8	Alt-tide gauge 1993.0-2018.0
PERT	$-0.62 \pm 0.00(2)$	-0.62 ± 0.52		
HIL1/HILS	-1.20 ± 0.45	-1.94 ± 0.53	-3.21 ± 1.53	-3.63 ± 0.26
CUAI	-0.08 ± 0.38	-0.78 ± 0.60		
FREM	$+0.45 \pm 0.40$		-2.09 ± 1.48	-1.66 ± 0.38
HILS – FREM difference	-1.65 ± 0.60		-1.12 ± 2.38	-1.97 ± 0.42

530
 531 Table 3: Multi-technique VLM rates for each site (including HILS – FREM VLM
 532 difference). All units are mm/yr.

533
 534 To investigate the possible non-linearity of VLM at these sites, we have shown
 535 longer term (1993.0-2018.0) rates for altimetry minus tide gauge (Table 3) and cGPS VLM
 536 (various periods; Table 4)., These are also plotted in Figure 5, and suggest that the rates
 537 shown here are dependent on the time period used, indicating non-linearity (cf. Burgette et al.
 538 2013; Merrifield and Thompson 2018). This is most evident at PERT, where the 2012.8-
 539 2017.8 cGPS rate is -0.62 ± 0.52 mm/yr (Table 3), but for 1996.0-2019.3 (Table 4) is –
 540 2.22 ± 0.33 mm/yr computed using CATS for this study (from NGL data), which is in
 541 reasonable agreement with -2.09 ± 0.38 (1995.0-2014.0) for ULR6 (Santamaria-Gomez et al.
 542 2017) and -2.34 ± 0.59 (1996.0-2019.3) for MIDAS (Blewitt et al. 2016). Non-linearity is less
 543 obvious at HIL1 (-1.94 ± 0.53 mm/yr compared to -2.36 ± 0.27 mm/yr for 1996.0-2019.3),
 544 although this location has been shown by Featherstone et al. (2015) to have undergone non-
 545 linear subsidence due to increased groundwater extraction in the early 2000s. We computed
 546 HIL1 cGPS rates as -2.36 mm/yr using CATS and NGL data, compared to -2.78 ± 0.31 mm/yr
 547 (2005.0-2014.0) for ULR6 (Santamaria-Gomez et al. 2017) and -2.69 ± 0.62 mm/yr (1997.7-
 548 2019.3) from MIDAS (Blewitt et al. 2016).

549

Site	cGPS (mm/yr)
PERT (NGL) 1996.0-2019.3	-2.22 ± 0.33
PERT (ULR6) 1995.0-2014.0	-2.09 ± 0.38
PERT (MIDAS) 1996.0-2019.3	-2.34 ± 0.59
HIL1/HILS (NGL) 1996.0-2019.3	-2.36 ± 0.27
HIL1 (ULR6) 2005.0-2014.0	-2.78 ± 0.31
HIL1 (MIDAS) 1997.7-2019.3	-2.69 ± 0.62

550

551 Table 4: Longer period rates for cGPS stations from NGL time series processed for this study
 552 in CATS, ULR6 (Santamaría-Gómez et al. 2017) and MIDAS (Blewett et al. 2016) .

553

554 The tide gauge minus altimetry VLM for the TSX period (2012.8 – 2017.8) is not
 555 statistically different to the 1993.0-2018.0 period, although this is partly due to the larger
 556 uncertainty in the TSX-period VLM. The difference between long-term HIL1 (-2.36 ± 0.27
 557 mm/yr) and HILS tide gauge minus altimetry (-3.63 ± 0.26 mm/yr) VLM is statistically
 558 significant, and although over slightly different periods (1996.0-2019.3 and 1993.0-2018.0
 559 respectively) suggests a bias between these techniques at the two tide gauges.

560 The difference between the two tide gauge's VLM from the InSAR and tide gauge
 561 minus altimetry as shown on the right-hand-side ('site' 5) of Figure 5 is important. The close
 562 proximity of these two sites (~30 km) allows the comparison of the differential VLM from
 563 these two independent techniques, and it indicates that they produce similar results, at least
 564 for this experiment. It suggests that while there may be offsets in one (or both) of these
 565 techniques, the differential VLM from each is in reasonably good agreement within
 566 uncertainty. The differential agreement between FREM and HILS for independent altimetry
 567 minus tide gauge and TSX, and also HIL1 and CUA1 indicates that the TSX phase ramp
 568 removes most of any long-wavelength atmospheric or orbital ramp that may have affected the
 569 TSX rates at Fremantle. Any remaining differences are most likely a combination of the
 570 uncertainty within the tide gauge, altimetry, cGPS and TSX measurements.

571

572 **4. Conclusion**

573 Differential VLM rates from TSX appear to deliver similar precision to that estimated from
574 first order differential levelling in the study of Lyon et al. (2018; both around ± 0.4 mm/yr to
575 ± 0.5 mm/yr), although this is dependent on the time period and number of observations in
576 each. Differential TSX rates give a reasonable agreement with tide gauge minus altimetry
577 differential VLM between the two tide gauges, supporting the TSX processing methods and
578 removal of long-wavelength systematic errors by the phase ramp. When comparisons are
579 made for the 2012.8 – 2017.8 period among VLM rates from TSX referenced to IGS08 at
580 PERT, altimetry minus tide gauge and cGPS rates in IGS08, there appear to be systematic
581 offsets. It is not yet clear if this is the limit of the techniques' precision, the result of
582 systematic differences between the techniques, or their accuracy within their respective
583 reference frames over this shorter time period.

584 TSX VLM at FREM referenced to IGS08 at PERT cGPS is $+0.45 \pm 0.40$ mm/yr for
585 2012.8-2017.8. This slight uplift is different to long-term subsidence rates of -1.66 mm/yr
586 from tide gauge minus altimetry for 1993-2018, suggesting non-linear VLM at FREM.
587 However, this should be viewed cautiously considering the possibility of a systematic bias of
588 up to 1 mm/yr in the tide gauge minus altimetry VLM rate, and also that when approximate
589 TRF cGPS uncertainties are propagated into the TSX rates, these (probably upper bound)
590 uncertainties can approach ± 1 mm/yr.

591 These InSAR results suggest that when longer time series are acquired over more tide
592 gauges, InSAR may provide remotely sensed estimates of differential VLM for tide gauge
593 'geodetic ties' that could be extended globally. The need for geodetic ties for global tide
594 gauges to support sea level studies is made by Woodworth et al (2017, and others), so that the
595 continued acquisition of InSAR to build long time series over tide gauges is of high
596 importance to facilitate more detailed tide gauge VLM analyses in the future.

597 **Acknowledgments**

598 We would like to thank the following organisations for providing and/or funding these data.
599 TerraSAR-X scenes are acquired under the German Space Center's (DLR's) Science Project
600 LAN1499, funded by AuScope under the Australian Geophysical Observing System
601 (AGOS), and Australian Research Council (ARC) Linkage Projects LP 110100284 and
602 LP140100155. The Ssalto/Duacs altimeter products were produced and distributed by the
603 Copernicus Marine and Environment Monitoring Service (CMEMS)
604 (<http://marine.copernicus.eu>). Dynamic atmospheric Corrections are produced by CLS using
605 the Mog2D model from Legos and distributed by Aviso+, with support from CNES
606 (<https://www.aviso.altimetry.fr/>). GPS data was obtained from Nevada Geodetic Laboratory
607 at <http://geodesy.unr.edu/>. Monthly sea level means were obtained from the Permanent
608 Service for Mean Sea Level (PSMSL) <https://psmsl.org/>. We would also like to thank
609 Professor Andy Hooper for making StaMPS software freely available and the Delft
610 University of Technology for providing the Doris software. Figures 1-5 were plotted using
611 the Generic Mapping Tools (Wessel et al. 2013)

612

613 **Data availability**

614 The TerraSAR-X scenes are available to us under licence through DLR Science Project
615 LAN1499, so cannot be made publicly available.
616 ULR6 and NGL rates obtained from SONEL (<https://www.sonel.org/>). Processed GPS data
617 are freely available at Nevada Geodetic Laboratory <http://geodesy.unr.edu/>, and also SONEL
618 <https://www.sonel.org/-ULR-112-.html>.
619 Monthly sea level records are freely available at PSMSL <https://psmsl.org/>.
620 Altimetry data is available at CMEMS <http://marine.copernicus.eu>

621 Dynamic atmospheric corrections (DAC) are available from Aviso+ at

622 <https://www.aviso.altimetry.fr/>

623

624 **References**

625 Adamska LM (2012) Use of persistent scatterer interferometry for the enhancement of vertical land movement
626 measurement at tide gauges around the British coast. PhD thesis, University of Nottingham, UK.

627 Agram PS, Simons M (2015) A noise model for InSAR time series. *Journal of Geophysical Research: Solid*
628 *Earth*, 120(4):2752-2771, doi:10.1002/2014JB011271.

629 Altamimi Z, Collilieux X, Metivier L (2011) ITRF2008: An improved solution of the International Terrestrial
630 Reference Frame. *Journal of Geodesy*, 85(5): 457-473, doi:10.1007/s00190-011-0444-4.

631 Bekaert DPS, Hooper A, Wright TJ (2015) A spatially variable power-law tropospheric correction technique for
632 InSAR data. *Journal of Geophysical Research: Solid Earth*, 120(2):1345-1356, doi:10.1002/2014JB011558.

633 Bekaert DPS, Hamlington BD, Buzzanga B, Jones CE (2017) Spaceborne synthetic aperture radar survey of
634 subsidence in Hampton Roads, Virginia (USA). *Science Reports*, 7: 14752, doi:10.1038/s41598-017-15309-
635 5.

636 Bevis M, Scherer W, Merrifield M (2002) Technical issues and recommendations related to the installation of
637 continuous GPS stations at tide gauges. *Marine Geodesy*, 25(1-2): 87-99,
638 doi:10.1080/014904102753516750.

639 Blewitt G, Kreemer C, Hammond WC, Gazeaux J (2016) MIDAS robust trend estimator for accurate GPS
640 station velocities without step detection. *Journal of Geophysical Research: Solid Earth*, 121(3): 2054-2068,
641 doi:10.1002/2015JB012552.

642 Blewitt G, Hammond WC, Kreemer C (2018) Harnessing the GPS data explosion for interdisciplinary science,
643 *EOS – Transactions of the American Geophysical Union*, 99, doi: 10.1029/2018EO104623.

644 Brooks BA, Merrifield MA, Foster J, Werner CL, Gomez F, Bevis M, Gill S (2007) Space geodetic
645 determination of spatial variability in relative sea level change, Los Angeles basin. *Geophysical Research*
646 *Letters*, 34(1), L01611, doi:10.1029/2006GL028171.

647 Burgette R, Watson CS, Church JA, Tregoning P, Coleman R (2013), Characterizing and minimizing the effects
648 of noise in tide gauge time series: Relative and geocentric sea level rise around Australia, *Geophysical*
649 *Journal of International*, 194(2): 719-736, doi:10.1093/gji/ggt131.

- 650 Cao·Y, Li Z, Wei·J, Hu J, Duan M, Feng G (2018) Stochastic modeling for time series InSAR: with emphasis
 651 on atmospheric effects. *Journal of Geodesy*, 92(2):185–204, doi.org/10.1007/s00190-017-1055-5
- 652 Dheenathayalan P, Small D, Schubert A, Hanssen RF (2016) High-precision positioning of radar scatterer.
 653 *Journal of Geodesy*, 90(5): 403-422, doi: 10.1007/s00190-015-0883-4.
- 654 Dheenathayalan P, Cuenca MC, Hoogeboom P, Hanssen RF (2017) Small reflectors for ground motion
 655 monitoring with InSAR. *IEEE Transactions on Geoscience and Remote Sensing*, 55(12): 6703-6712, doi:
 656 10.1109/TGRS.2017.2731424.
- 657 Fattahi H, Amelung F (2014) InSAR uncertainty due to orbital errors. *Geophysical Journal International*,
 658 199(1), 549–560, doi: 10.1093/gji/ggu276.
- 659 Fattahi H, Amelung F (2015) InSAR bias and uncertainty due to systematic and stochastic tropospheric delay.
 660 *Journal of Geophysical Research: Solid Earth*, 120(12):8758-8773, doi:10.1002/2015JB012419.
- 661 Featherstone WE, Penna NT, Filmer MS, Williams SDP (2015) Nonlinear subsidence at Fremantle, a long-
 662 recording tide gauge in the Southern Hemisphere. *Journal of Geophysical Research: Oceans* 120(10): 7004-
 663 7014, doi: 10.1002/2015JC011295.
- 664 Ferretti A, Prati C, Rocca F (2001) Permanent scatterers in SAR Interferometry. *IEEE Transactions on*
 665 *Geoscience and Remote Sensing*, 39(1): 8-20, doi: 10.1109/36.898661
- 666 Fielding EJ, Blom RG, Goldstein RM (1998) Rapid subsidence over oil fields measured by SAR interferometry.
 667 *Geophysical Research Letters*, 25(17): 3215-3218, doi: 10.1029/98GL52260
- 668 Garthwaite M (2017) On the design of radar corner reflectors for deformation monitoring in multi-frequency
 669 InSAR. *Remote Sensing*, 9(7): 648, doi:10.3390/rs9070648.
- 670 Gomba G, Gonzalez FR, De Zan F (2017) Ionospheric Phase Screen Compensation for the Sentinel-1 TOPS and
 671 ALOS-2 ScanSAR Modes. *IEEE Trans. Geosci. Remote Sens.* 55 (1), 223-235.
- 672 Hamlington BD, Thompson P, Hammond WC, Blewitt G, Ray RD (2016) Assessing the impact of vertical land
 673 motion on twentieth century global mean sea level estimates. *Journal of Geophysical Research Oceans*,
 674 121(7): 4980-4993, doi: 10.1002/2016JC011747.
- 675 Hammond WC, Burgette RJ, Johnson KM, Blewitt G. (2018) Uplift of the Western Transverse Ranges and
 676 Ventura Area of Southern California: A four-technique geodetic study combining GPS, InSAR, levelling,
 677 and tide gauges *Journal of Geophysical Research - Solid Earth*, 123(1): 836–858, doi:
 678 10.1002/2017JB014499.
- 679 Hanssen RF (2001). *Radar Interferometry: Data Interpretation and Error Analysis*, Kluwer, Academic.

- 680 Holgate SJ, Matthews A, Woodworth PL, Rickards LJ, Tamisiea ME, Bradshaw E, Foden PR, Gordon KM,
681 Jevrejeva S, Pugh J (2013) New data systems and products at the permanent service for mean sea level,
682 *Journal of Coastal Research*, 29(3), 493-504, doi:10.2112/JCOASTRES-D-12-00175.1.
- 683 Hooper A (2008) A multi-temporal InSAR method incorporating both persistent scatterer and small baseline
684 approaches. *Geophysical Research Letters*, 35(16):L16302, doi: 10.1029/2008GL034654.
- 685 Hooper A, Zebker HA (2007) Phase unwrapping in three dimensions with application to InSAR time series.
686 *Journal of the Optical Society of America A*, 24(9): 2737-2747, doi: 10.1364/JOSAA.24.002737.
- 687 Hooper A, Bekaert D, Spaans K, Arikian M (2012), Recent advances in SAR interferometry time series analysis
688 for measuring crustal deformation. *Tectonophysics*, 514–517: 1-13, doi:10.1016/j.tecto.2011.10.013.
- 689 Kampe, B (2006). Radar interferometry: persistent scatterer technique. Springer, Dordrecht.
- 690 Kampes B, Usai S (1999) Doris: The Delft object-oriented Radar Interferometric software. In: proceedings ITC
691 2nd ORS symposium, August.
- 692 King MA, Keshin M, Whitehouse PL, Thomas ID, Milne M, Riva RE (2012) Regional biases in absolute sea-
693 level estimates from tide gauge data due to residual unmodeled vertical land movement. *Geophysical*
694 *Research Letters*, 39(14), L14604, doi:10.1029/2012GL052348.
- 695 Kuo CY, Shum CK, Braun A, Mitrovica JX, (2004) Vertical crustal motion determined by satellite altimetry and
696 tide gauge data in Fennoscandia. *Geophysical Research Letters*, 31(1): L01608,
697 doi:10.1029/2003GL019106.
- 698 Le Cozannet G, Raucoules D, Wöppelmann G, de Michele M, Poupardin A (2014) InSAR monitoring of ground
699 motions impacts for in-situ sea level measurement: the example of Dakar (Senegal). IGARSS, Quebec City,
700 QC, Canada, 13-18 July 2014, doi: 10.1109/IGARSS.2014.6946588
- 701 Le Cozannet G, Raucoules D, Wöppelmann G, Garcin M, Da Sylva S, Meyssignac B, Gravelle M, Lavigne F
702 (2015) Vertical ground motion and historical sea-level records in Dakar (Senegal). *Environmental Research*
703 *Letters*, 10: 084016, doi: 10.1088/1748-9326/10/8/084016.
- 704 Lyon TJ, Filmer MS, Featherstone WE (2018) On the use of repeat leveling for the determination of vertical
705 land motion: artifacts, aliasing and extrapolation errors. *Journal of Geophysical Research: Solid Earth*,
706 123(8):7021-7039, doi: 10.1029/2018JB015705.
- 707 Mahapatra P, Samiei-Esfahany S, van der Marel H, Hanssen R (2014) On the Use of Transponders as Coherent
708 Radar Targets for SAR Interferometry. *IEEE Transactions on Geoscience and Remote Sensing*, 52(3): 1869,
709 doi: 10.1109/TGRS.2013.2255881.

- 710 Mahapatra P, van der Marel H, van Leijen F, Samiei-Esfahany S, Klees R, Hanssen R (2018) InSAR datum
711 connection using GNSS-augmented radar transponders. *Journal of Geodesy*, 92(1):21–32,
712 doi:10.1007/s00190-017-1041-y.
- 713 Mazzotti S, Jones C, Thomson RE (2008) Relative and absolute sea level rise in western Canada and
714 northwestern United States from a combined tide gauge-GPS analysis. *Journal of Geophysical Research -*
715 *Oceans*, 113, C11019, doi:10.1029/2008JC004835.
- 716 Merrifield MA, Thompson PR (2018) Interdecadal sea level variations in the Pacific: Distinctions between the
717 tropics and extratropics. *Geophysical Research Letters*, 45(13):6604-6610, doi: 10.1029/2018GL077666
- 718 Parker AL, Filmer MS, Featherstone WE (2017) First results from Sentinel-1A InSAR over Australia:
719 Application to the Perth Basin. *Remote Sensing* 9(3): 299; doi: 10.3390/rs9030299.
- 720 Peltier WR (2004) Global glacial isostasy and the surface of the ice-age Earth: The ICE-5G (VM2) Model and
721 GRACE, *Annual Review of Earth and Planetary Sciences*, 32: 111-149, doi:
722 10.1146/annurev.earth.32.082503.144359.
- 723 Pfeffer J, Allemand P (2016) The key role of vertical land motions in coastal sea level variations: A global
724 synthesis of multisatellite altimetry, tide gauge data and GPS measurements. *Earth and Planetary Science*
725 *Letters*, 439: 39-47, doi: 10.1016/j.epsl.2016.01.027.
- 726 Poitevin C, Wöppelmann G, Raucoules D, Le Cozannet G, Marcos M, Testut L (2019) Vertical land motion and
727 relative sea level changes along the coastline of Brest (France) from combined space-borne geodetic
728 methods *Remote Sensing of Environment*, 222: 275-285, doi:10.1016/j.rse.2018.12.035
- 729 Raucoules D, Le Cozannet G, Wöppelmann G, de Michele M, Gravelle M, Daag A, Marcos M (2013) High
730 nonlinear urban ground motion in Manila (Philippines) from 1993 to 2010 observed by DInSAR:
731 implications for sea-level measurements. *Remote Sensing of Environment*, 139:386-397,
732 doi:10.1016/j.rse.2013.08.021.
- 733 Rucci A, Ferretti A, Monti Guarnieri A, Rocca F (2012) Sentinel 1 SAR interferometry applications: The
734 outlook for sub millimeter measurements. *Remote Sensing of Environment*, 120:156-163, doi:
735 10.1016/j.rse.2011.09.030.
- 736 Santamaría-Gómez A, Gravelle M, Dangendorf S, Marcos M, Spada G, Wöppelmann G (2017) Uncertainty of
737 the 20th century sea-level rise due to vertical land motion errors, *Earth and Planetary Science Letters*, 473:
738 24–32, doi: 10.1016/j.epsl.2017.05.038.
- 739 Vaniček P, Castle RO, Balaz, EI (1980) Geodetic levelling and its applications. *Reviews of Geophysics and*

- 740 *Space Physics*. 18(2), 505–524. <https://doi.org/10.1029/RG018i002p00505>.
- 741 Wessel P, Smith WHF, Scharroo R, Luis J, Wobbe F (2013) Generic Mapping Tools: Improved Version
 742 Released. *Eos, Transactions, American Geophysical Union*, 94(45):409–420,
 743 <https://doi.org/10.1002/2013EO450001>
- 744 Williams SDP (2003) The effect of coloured noise on the uncertainties of rates estimated from geodetic time
 745 series. *Journal of Geodesy* 76 (9–10), 483–494. <https://doi.org/10.1007/s00190-002-0283-4>.
- 746 Williams SDP. (2008), CATS: GPS coordinate time series analysis software, *GPS Solutions*, 12(2), 147–153,
 747 doi: 10.1007/s10291-007-0086-4.
- 748 Williams S, Bock Y, Fang P (1998) Integrated satellite interferometry: Tropospheric noise, GPS estimates and
 749 implications for interferometric synthetic aperture radar products, *Journal of Geophysical Research –Solid*
 750 *Earth*, 103(B11): 27,051–27,067, doi:10.1029/98JB02794.
- 751 Woodworth, PL (2012) A note on the nodal tide in sea level records. *Journal of Coastal Research*, 28 (2), 316–
 752 323, doi: 10.2112/JCOASTRES-D-11A-00023.1
- 753 Woodworth PL, Wöppelmann G, Marcos M, Gravelle M, Bingley RM (2017) Why we must tie satellite
 754 positioning to tide gauge data. *EOS – Transactions of the American Geophysical Union*, 98 (4): 13–15, doi:
 755 10.1029/2017EO064037.
- 756 Woodworth PL, Melet A, Marcos M, Ray RD, Wöppelmann, G., Sasaki YN, Cirano M, Hibbert A, Huthnance
 757 JM, Monserrat S, Merrifield MA (2019) Forcing factors affecting sea level changes at the coast. *Surveys in*
 758 *Geophysics*, doi: 10.1007/s10712-019-09531-1.
- 759 Wöppelmann G, Martin Miguez B, Bouin MN, Altamimi Z (2007) Geocentric sea-level trend estimates from
 760 GPS analyses at relevant tide gauges world-wide, *Global and Planetary Change*, 57(3–4), 396–406,
 761 doi:10.1016/j.gloplacha.2007.02.002
- 762 Wöppelmann G, Le Cozannet G, De Michele M, Raucoules D, Cazenave A, Garcin M, Hanson S, Marcos M,
 763 Santamaría-Gómez, A (2013) Is land subsidence increasing the exposure to sea level rise in Alexandria,
 764 Egypt? *Geophysical Research Letters*, 40 (12): 2953–2957, doi: 10.1002/grl.50568.
- 765 Wöppelmann G, Marcos M (2016) Vertical land motion as a key to understanding sea level change and
 766 variability. *Reviews of Geophysics*, 54 (1): 64–92, doi: 10.1002/2015RG000502.
- 767